View metadata, citation and similar papers at core.ac.uk

brought to you by CORE

provided by University of Montana

University of Montana

ScholarWorks at University of Montana

Undergraduate Theses and Professional Papers

2017

Using Thermal Infrared Imagery To Estimate Soil Hydraulic Parameters: A Novel Approach

Matthew B. Thomas
University of Montana, Missoula, thomas.matt0@gmail.com

Follow this and additional works at: https://scholarworks.umt.edu/utpp

 Part of the Hydrology Commons, and the Soil Science Commons

Let us know how access to this document benefits you.

Recommended Citation

Thomas, Matthew B., "Using Thermal Infrared Imagery To Estimate Soil Hydraulic Parameters: A Novel Approach" (2017). *Undergraduate Theses and Professional Papers*. 173.
https://scholarworks.umt.edu/utpp/173

This Thesis is brought to you for free and open access by ScholarWorks at University of Montana. It has been accepted for inclusion in Undergraduate Theses and Professional Papers by an authorized administrator of ScholarWorks at University of Montana. For more information, please contact scholarworks@mso.umt.edu.

USING THERMAL INFRARED IMAGING TO ESTIMATE SOIL HYDRAULIC PARAMETERS: A NOVEL APPROACH

By

MATTHEW BARKER THOMAS

Undergraduate Thesis
presented in partial fulfillment of the requirements
for the University Scholar distinction

Davidson Honors College
University of Montana
Missoula, MT

Official Graduation Date May 2017

Approved by:

W. Payton Gardner, Faculty Mentor
Marco Maneta, Faculty Mentor
Department of Geosciences

ABSTRACT

Thomas, Matthew, B.S., May 2017 Geosciences

Using Thermal Infrared Imaging to Estimate Soil Hydraulic Parameters: A Novel Approach

Faculty Mentor: W. Payton Gardner, Marco Maneta

In this study, skin temperature measured with a thermal infrared (TIR) camera was used to estimate soil hydraulic parameters. These physical properties that control how soils transport and retain water are notoriously difficult to measure in the field due to spatial variability. Laboratory experiments were set up to record surface skin temperature response in a clean soil column using a TIR camera after an artificial wetting event. An array of thermocouples, a net radiometer, heat flux sensor and weather station were used to constrain the TIR data and the energy budget during the experiment. The soil column surface was then wetted with a known amount of water over a controlled time period and the thermal response recorded at five minute intervals over the course of 18 hours. Soil hydraulic parameters were then estimated by fitting a water-energy conservation model (ECH_2O) to the observed data using a Marqhart-Levenberg least squares minimization method. The estimated parameters obtained were then compared to several sets of known values based on soil textural classification. This inversion of ECH_2O was able to estimate the Brooks-Corey λ for sand with a relatively high degree of precision; however, the inversion was unable to provide reasonable estimates of air entry pressure for sand, air entry pressure for soil, or the Brooks-Corey λ for soil. These results indicate that soil hydraulic parameter estimation based on TIR skin temperature data could potentially be a fast and useful new tool to characterize the distribution and spatial heterogeneity in some soil hydraulic parameters. However, future studies should test the method with dedicated groundwater flow models and accurately account for surface emissivity before conducting field tests.

Table of Contents

Figures

Tables

Using Thermal Infrared Imaging to Estimate Soil Hydraulic Parameters: A Novel Approach

Introduction

Fluid transport and storage in the vadose zone is a key part of the hydrologic cycle, and is an important aspect of critical zone science. The multi-phase nature of the vadose zone system leads to highly nonlinear models that relate various soil properties and state variables. Two of the most common water retention models are the Brooks-Corey model (Equation 1) and the van Genuchten model (Equation 2).

$$\theta = \left(\frac{\psi_{ae}}{\psi}\right)^{\frac{1}{\lambda}} n \qquad (1)$$

$$\theta = \theta_r + \frac{\theta_s - \theta_r}{\left[1+\alpha\psi^{\beta}\right]^{1-\frac{1}{\beta}}} \qquad (2)$$

Where θ is volumetric soil water content, ψ_{ae} is the soil air entry pressure (m), ψ is soil tension (m), λ is the Brooks-Corey pore size distribution parameter, n is porosity, θ_r is residual soil water content, θ_s is saturated soil water content, and α and β are fitting parameters (Brooks and Corey 1964, van Genuchten 1980).

The inherent complexity of this system has led to the widespread use of numerical modeling to simulate fluid flow and storage. These models require accurate measurements of the soil hydraulic properties and parameters (SHPs) that control transport (Mertens 2005). These properties often exhibit a high degree of spatial heterogeneity, making high precision modeling a difficult task. For instance, Scholl and Christenson (1998) found hydraulic conductivity (K_s) to vary three orders of magnitude along a 215 m transect. Similarly, infiltration rates, controlled by SHPs, have been found to vary up to two orders of magnitude at the hectare scale (Sharma et al 1980). At the field scale, large areas are often simply assigned uniform SHP values based off a single measurement or the textural properties of the soil, when in reality a large number of in situ measurements must be made to properly characterize field heterogeneity (Pedretti et al 2012, Clancy and Alba 2011). New methodologies that can quickly characterize SHPs and their spatial heterogeneity to properly parameterize numerical models are needed (Dane et al 2002).

Traditional field measurement methods of SHPs often rely on covered cylinder infiltrometer experiments (Bouwer 1966). Parameters that cannot directly be measured with this

technique can be calculated by empirical models that take infiltrometer measurements as input (Fallow 1994). However, these devices are prone to user error and have many issues associated with them (Bouwer 1986). Additionally, they only provide point measurements, requiring a systematic and repeated infiltrometer campaign to characterize heterogeneity.

At the other end of the spatial scale is the application of remote sensing methods to measure SHPs. Infrared and microwave remote sensing data have long been used to measure soil moisture content and thermal inertia (Price 1980, Petropoulos et al 2015). Recently, some researchers have tried to use remote sensing to measure SHPs as well. Cohen et al (2007) were able to use near infrared (NIR) spectroscopy to estimate K_s with a moderate degree of accuracy. Minasny et al (2008) determined that K_s could not be estimated accurately using mid infrared (MIR) spectroscopy. Babaeian et al 2015 were able to show correlation between spectral reflectance values and the α^* fitting parameter, n fitting parameter, saturated hydraulic conductivity, and saturated volumetric water content parameters of the Mualem-van Genuchten model. Gutmann and Small (2010) calibrated MODIS surface temperature data to the Noah land surface model to estimate K_s and the m parameter of the van Genuchten model. However, these methods suffer from coarse spatial resolution on the scale of kilometers. Their study was focused on large spatial scales to estimate Land Hydraulic Properties (LHPs) and only had two isolated temperature data points around midday per day to fit the Noah outputs to. Finer resolution is necessary to study many surface processes (Fang and Lakshmi 2014).

A promising method to obtain SHPs at fine spatial scales is the use of fiber optic Distributed Temperature Sensing (DTS). These cables measure soil temperature at 1 m resolution along their entire length, which can exceed 10 km with current technology. DTS has the potential to accurately estimate soil moisture content as a function of soil temperature, as well as K_s via inverse modeling (Dong et al 2016). However, both active and passive DTS are inherently invasive due to the need to bury the cables and disrupt the soil structure, a time consuming and labor intensive process. Active DTS has a large power requirement as well (Steele-Dunne et al 2010). In addition, DTS only provide temperature along a linear array. A more broadly distributed method of intermediate spatial resolution is needed.

The results of the study by Gutmann and Small show the potential of using skin temperature data and inversion modeling to estimate SHPs. However, a method which provides

this estimate at intermediate spatial resolution and scale is needed. Skin surface temperature measured from thermal infrared imagery could be an ideal methodology at a variety of spatial and temporal scales. In this paper, the utility of surface skin temperature data acquired with a TIR camera to estimate SHPs is tested. This method has the potential to estimate spatially distributed SHP, and bridge the scale gap between point and satellite footprint scales in SHP measurement.

Methods

To test the effectiveness of using TIR acquired skin temperature data to model SHPs, a controlled environment was constructed and wetting experiments were performed with different soil types. The environment was then simulated with a numerical model that coupled the mass and energy balance of the soil surface. An inversion modeling method was then used to fit this model to the observed data and estimate air-entry pressure and the Brooks-Corey λ.

Experiment

A laboratory experiment was setup to test the effectiveness of measuring soil skin temperature as a means to model SHPs. A 36 cm tall, 5 gallon bucket was filled to a height of 33 cm with soil material and a 1500 W heat lamp was placed 68 cm above the soil material surface to simulate daytime solar flux. To provide turbulence, a fan was directed at the bucket such that the wind was parallel to the soil material surface. Soil moisture sensors were installed at 10 cm, 17.5 cm, and 27.25 cm depth. Two thermocouples were placed at a depth of 10 cm and 0.5 cm, a heat flux plate was placed at a depth of 5 cm, and a net radiometer was placed just above and adjacent to the bucket (Figure 1). Ambient temperature and relative humidity were monitored with a meteorological station placed adjacent to the bucket. Wind speed was measured at 44 cm height above the surface with a handheld anemometer.

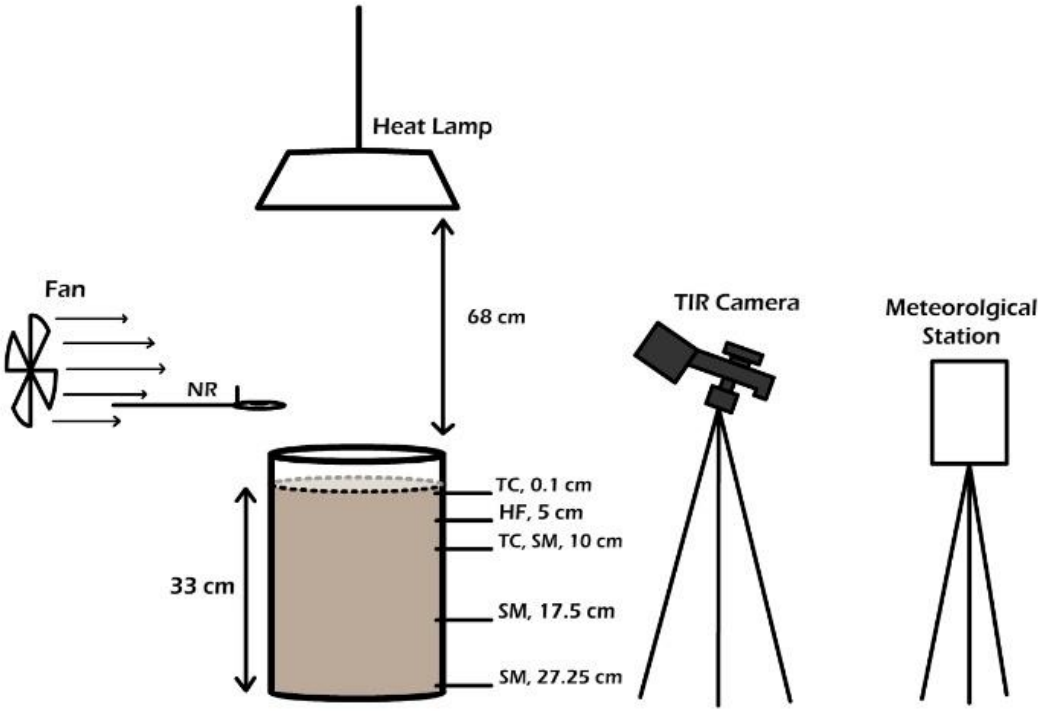

Figure 1: Diagram showing the major components of the experiment. TC = thermocouple, HF = heat flux plate, SM = soil moisture sensor

After allowing the soil material to arrive at an equilibrium temperature under the heat lamp over the course of several days, 910 mL of water at a temperature of 21.3 ºC was applied to the soil material over a period of 3.5 minutes as a fine mist to prevent disruption of the soil structure. The bucket was then allowed to dry out to observe the skin temperature recovery curve, with all data collected at 5 minute intervals.

Skin temperature data were collected with both a traditional thermocouple and a FLIR E8 TIR camera. This model included 320x240 resolution, thermal sensitivity of <0.06 °C, and a 45°x34° field of view. The camera was mounted on a tripod adjacent to the bucket (see Figure 1). The camera used required manual trigger operation to take images. Enabling the TIR camera to take images without an operator present was one of the major design challenges of this project. A tripod mount attachment for the FLIR E8 camera was downloaded from an online open source digital design file repository to hold the camera stationary for the experiment and modified with an additional raised platform to the tripod adapter. A high-torque servo motor and Arduino Uno microcontroller were secured to the raised platform. String was threaded through a

hole in the arm of the servo motor and around the trigger on the TIR camera. The microcontroller was programmed to have the motor rotate the arm up 30° and back down to its original position on a 5 minute recurrence interval. The servo motion caused the string to squeeze the trigger and take an image (Figure 2). To prevent overloading the microcontroller, both the servo and the microcontroller were supplied power through different inputs. Both devices had to be wired to a common ground to close the circuit. This left the signal wire as the only direct connection between the motor and the microcontroller.

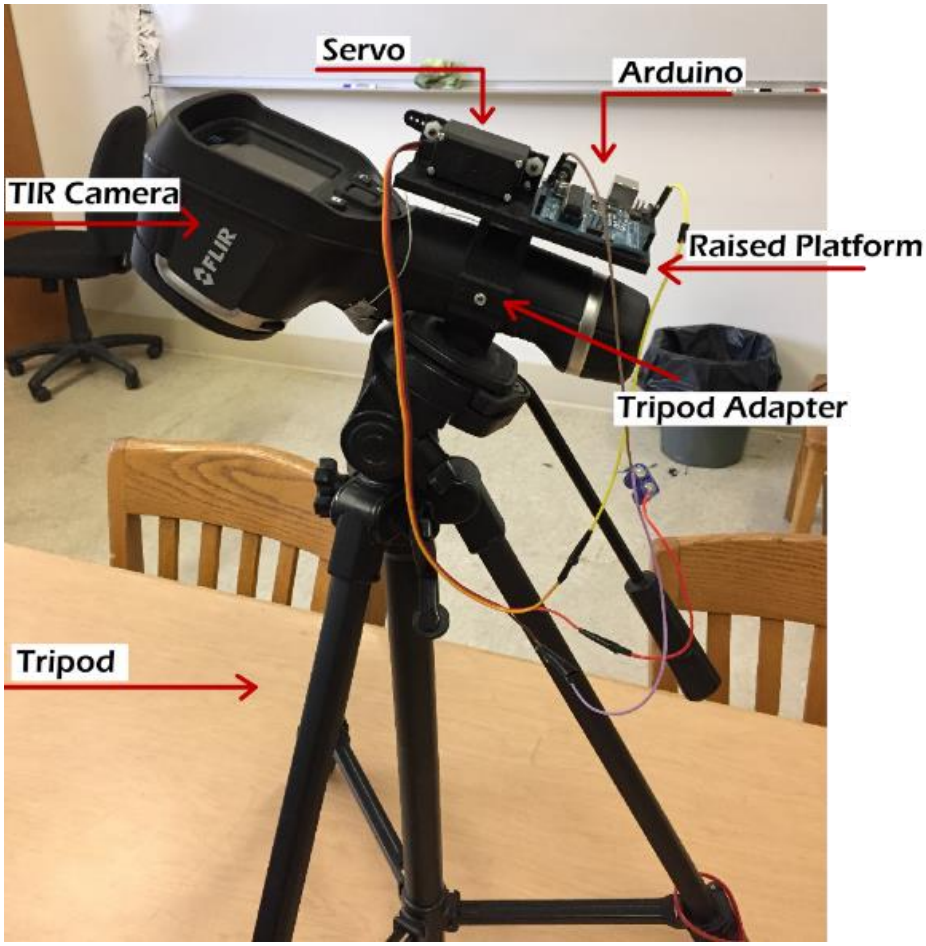

Figure 2: Automated camera design

After the experiment, skin temperature data from the TIR camera were compiled into a .csv file. Skin temperature data for each image was compiled using the FLIR Tools software to create a .csv file for each individual image. These files were then indexed in an external program that read values from the same group of pixels centered over the skin temperature thermocouple

in each image and calculated an average (Figure 3). The average value for the given area for each image was then written to a new .csv file indexed by the image time.

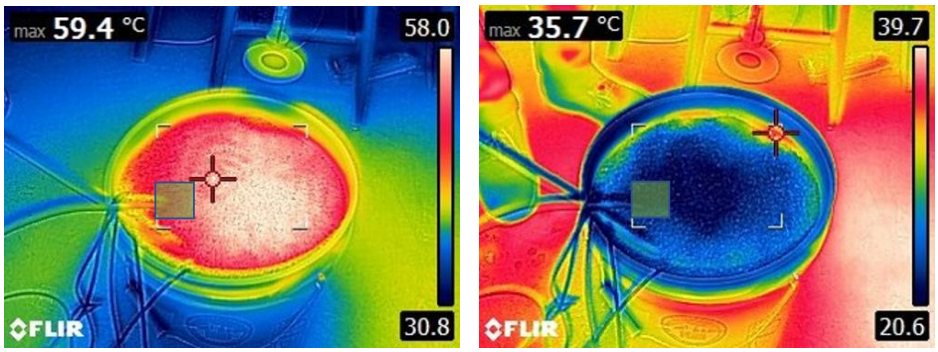

Figure 3: IR images from before (left) and after (right) water application. The pixels used to calculate an average temperature are highlighted in green.

Modeling

The ECH_2O ecohydrologic model (Maneta and Silverman, 2013) was used to simulate a bare, unvegetated surface with no topography. ECH_2O is a spatially distributed numerical model that couples the vertical energy balance equation for a two-layer system to a hydrologic and forest/vegetation growth model. The vertical energy balance uses a surface and a canopy layer; however, for this study no vegetation was simulated and the canopy layer and forest growth model were not considered.

Theory

The governing equation for the 1-D vertical transport of water in the subsurface is:

$$S_s \frac{\partial H}{\partial t} = -\frac{\partial(-K_z \frac{\partial H}{\partial z})}{\partial z} \quad (3)$$

where S_s is the specific storage (m^{-1}), H is the hydraulic head (m), t is time (s), K_z is hydraulic conductivity in the z-direction (ms^{-1}), and z is depth (m). The 1-D kinematic wave approximation of this equation, assuming homogenous conditions, is (Singh, 1997):

$$\frac{\partial H}{\partial t} + Ksin(S_x)\frac{\partial H}{\partial z} = R \quad (4)$$

where S_x is the slope in the x direction and R accounts for all sources and sinks of water in the domain. In this simulation, $S_x = 0$ and there are no sources or sinks within the domain itself. This

is the form of the groundwater flow equation implemented in ECH$_2$O with an implicit first order finite difference numerical method. The model avoids having sin(S_x) = 0 by forcing a nonzero minimum slope in the calculation. Infiltration is implemented as a form of the Green and Ampt equation:

$$I_f = K_s[\frac{\psi_{ae}(1-S_\theta)n}{\theta d_s} + 1] \qquad (5)$$

Where I_f is the infiltration rate (ms^{-1}), ψ_{ae} is the soil air entry pressure (m), S_θ is effective saturation, n is porosity, θ is the volumetric soil water content for the soil layer, and d_s is the depth of the hydrologically active soil layer. Potential infiltration (F_p), given as a depth of water, is calculated as

$$F_p = \min(h_w, I_f t_p) \quad (6)$$

where h_w is the ponding depth on the surface (m) and t_p is the time at which ponding occurs (s). Actual infiltration (ΔF) is given as a depth of water by

$$\Delta F = \Delta\theta d_s = F_p + K_s(\Delta t - t_p) - \psi\Delta\theta \times \ln(\frac{\psi\Delta\theta + \Delta\theta d_s}{\psi\Delta\theta + F_p}) \quad (7)$$

This equation is solved for Δθ iteratively by the Newton-Raphson method to find the increase of the average soil moisture over d_s that is now part of the subsurface reservoir and is governed by Equation 2.

The total energy balance for each pixel in the domain is:

$$R_n + H + G + R + E = 0 \quad (8)$$

Where R_n is net radiation, H is the sensible heat flux, G is the ground heat flux, R is sensible heat advected by rain, and E is the latent heat flux due to soil evaporation (all in W m^{-2}).

Net radiation is calculated by:

$$R_n = R_{s\downarrow}(1-\alpha) + \varepsilon_s R_L - \varepsilon_s \sigma T_s^4 \quad (9)$$

Where $R_{s\downarrow}$is shortwave radiation flux (Wm^{-2}), α is surface albedo, ε_s is surface absorptivity, R_L is longwave radiation flux (Wm^{-2}), σ is the Stefan-Boltzmann constant (Wm^{-2}K^{-4}), and T_s is the surface skin temperature (K).

The sensible heat flux is computed as:

$$H = \frac{\rho_a c_a}{r_{as}}(T_s - T_a) \quad (10)$$

Where ρ_a is the density of air (kg m^{-3}), c_a is the heat capacity of air (J m^{-3} K^{-1}), r_{as} is the aerodynamic resistance of the surface (s^{-1} m), and T_a is the air temperature (K). Sensible heat advected by precipitation is calculated as (Dingman 2002):

$$R = \rho_w c_w P_r (T_a - T_m), \quad (11)$$

where P_r is the precipitation rate (m s^{-1}) and T_m is the melting point of water (K).

The ground heat flux is calculated with (Arya 1988):

$$G = C_s(\theta) d_g \frac{\partial T}{\partial t} + G_{gp} \quad (12)$$

where G_p is flux across the surface (Wm^{-2}), G_{gp} is the heat flux (Wm^{-2}) at depth d_g, d_g is the depth of the top thermal layer boundary (.10 m), and $C_s(\theta)$ is the volumetric heat capacity of the soil (J m^{-3} K^{-1}). This is an analytical solution of the 1-D conductive heat flow governing equation:

$$\frac{\partial T}{\partial t} = \alpha \frac{\partial^2 T}{\partial z^2} \quad (13)$$

where T is temperature (K), t is time (s), α is the thermal diffusivity (m^{2}s^{-1}), and z is distance (m). G_{gp} is approximated by (Liebethal and Foken 2006)

$$G_{gp} = \sqrt{\frac{c_s(\theta) K_T(\theta) \pi}{P_e}}(T_d - T_s) \quad (14)$$

where P_e is the angular rotation speed of the Earth (s^{-1}), and T_d is the temperature of the lower thermal layer (K). In this simulation, $c_s(\theta)$ and $K_T(\theta)$ are calculated internally as a function of the soil moisture content at each timestep:

$$C_s(\theta) = (1-n)c_p\rho_p + \theta c_w \rho_w + (n-\theta)c_a\rho_a \quad (15)$$

$$K_T(\theta) = (1-n)K_p + \theta K_w + (n-\theta)K_a \quad (16)$$

where $K_T(\theta)$ is the bulk thermal conductivity (W m^{-1} K^{-1}), K_p, K_w, and K_a are the thermal conductivities of the surface, water, and air respectively, and c_p, c_w and ρ_p, ρ_w are the heat capacity (J m^{-3} K^{-1}) and density (kg m^{-3}) for the surface and water, respectively. A form of the Brooks-Corey equation is used to calculate θ in the vadose zone:

$$\theta = (\frac{\psi_{ae}}{\psi})^{\frac{1}{\lambda}} n \qquad (17)$$

Where ψ is soil tension (m) and λ is the Brooks-Corey pore size distribution parameter.

The soil evaporation term of the energy balance is:

$$E = \left(\frac{0.622\rho_a}{\lambda_v \rho_w P}\right)\left(\frac{k^2 v}{r_{as}}\right)(e_a - e_s RH_\theta) \qquad (18)$$

Where λ_v is the latent heat of vaporization of water (J g^{-1}), P is atmospheric pressure, k is the von Karman constant, e_a is the air vapor pressure (Pa), and e_s is the saturation vapor pressure (Pa). The saturation vapor pressure is modified by the RH_θ function to provide the soil pore relative humidity, with (Lee and Pielke 1992)

$$\int RH_\theta = \beta e_s T_s + (1-\beta) e_a T_a \qquad (19)$$

and β a function of soil moisture (Kondo et al 1990):

$$\beta = min\left\{1.0, \frac{1}{4}\left[1 - cos(\frac{\theta_{10}}{\theta_{fc}}\pi)^2\right]\right\} \qquad (20)$$

where θ_{10} is the soil moisture content of the top 10 cm of the soil column and θ_{fc} is field capacity.

Domain

A uniform, 100m x 100m domain with 30 cm grid resolution and a 33 cm deep soil layer with a flat surface, minimal rugosity, and no channels or drainage network was simulated with ECH_2O. The subsurface was divided into three layers of uniform properties, with partitions at 10 cm, 21.5 cm, and 33 cm depth (Figure 4). A single cell in the center of the domain was selected to simulate the column and output results. The column was devoid of any biological structures that would affect water and energy transport.

Initial conditions and boundary conditions

The soil column was set at an initial temperature of T_o = 23.5 °C at all depths and initial residual water content in each layer of $\theta_{1,2,3}$ = 0.05 for sand and θ_1 = 0.04, θ_2 = 0.09, θ_3 = 0.10 for potting soil. Once the model was started a constant radiative forcing of S = 995.0 Wm^{-2} was applied continuously. After 30 minutes had passed in the model, a precipitation input equivalent to the amount applied to the bucket was applied to the surface. The temperature at the lower boundary of the soil column was held constant at T_o. The side boundaries of the column were considered free flow boundaries, while the bottom of the column was considered a no flow boundary. All climate inputs to ECH_2O were derived from the observed data acquired with the meteorological station, anemometer, net radiometer. Table 1 shows the relevant spatially distributed parameters used for modeling each soil type; all other variables were related to ecological processes and were assigned the minimum possible value.

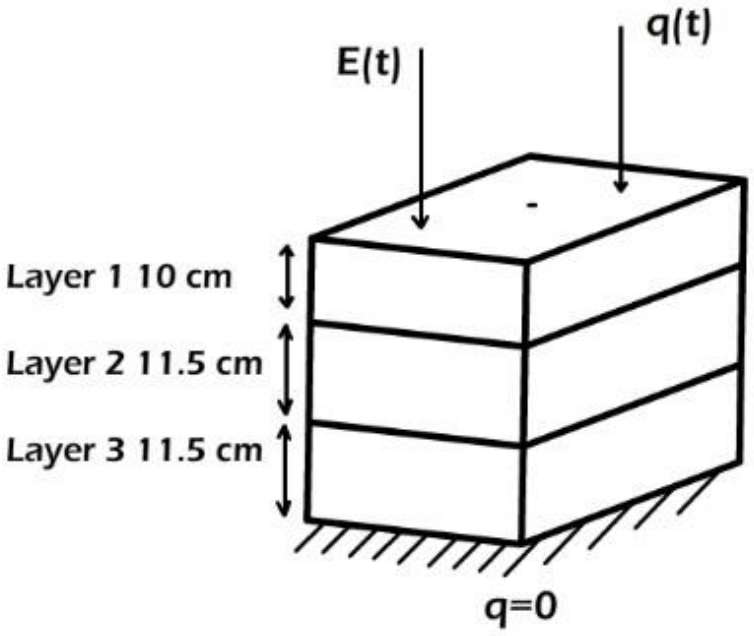

Figure 4: Domain and boundary conditions of model simulations

	Sand	Soil
Albedo	0.3	0.26
Emissivity	0.76	0.68
Soil heat capacity ($Jm^{-3}K^{-1}$)	830	700
Soil thermal conductivity ($Wm^{-1}K^{-1}$)	0.27	1.5
Damping depth (m)	0.34	0.34
Temperature at damping depth (°C)	61.0	46.0
Terrain rugosity (m)	0.05	0.05
K_s vertical-horizontal anisotropy ratio	1.0	1.0
Residual water content	0.05	0.01
Soil depth (m)	0.33	0.33
Effective hydraulic conductivity (ms^{-1})	0.000176	0.0000069
Porosity	0.4	0.45
Soil moisture, layer 1	0.05	0.011
Soil moisture, layer 2	0.05	0.099
Soil moisture, layer 3	0.05	0.124
Soil temperature (°C)	61.0	60.0
Depth, layer 1 (m)	0.10	0.10
Depth, layer 2 (m)	0.215	0.215
Leakance	0.0	0.0

Table 1: Spatial parameters input to ECH_2O for each soil type

Parameter Estimation

Model simulations using ECH_2O were run for 18 hours at 5 minute time steps. ψ_{ae} and λ values were then estimated by fitting the modeled output to the observed skin temperature data using a Marqhart-Levenburg least squares minimization.

Results

Sensitivity analysis

Sensitivity analyses were performed with ECH_2O to determine the degree to which SHPs controlled the modeled surface skin temperature. These analyses were performed for K_s, ψ_{ae}, and λ. For each parameter, five ECH_2O simulations were performed with a single parameter value increased while all other parameters were set to baseline values. Parameters were varied between a range of commonly reported values. After running the ECH_2O simulations, the difference

between the largest and smallest skin temperature values at each time step was normalized by the parameter range,

$$\frac{dT}{dP} = \frac{\max(t_i) - \min(t_i)}{R} \qquad (21)$$

where $\frac{dT}{dP}$ is the skin temperature sensitivity to parameter P, t_i is the i^{th} time step, and R is the range over which parameter P was varied. The results are shown in Figures 5-7.

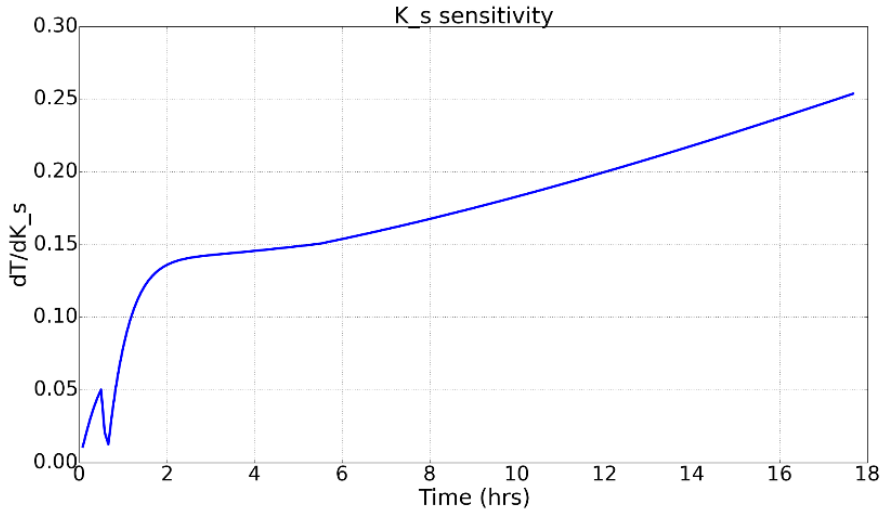

Figure 5: Sensitivity of skin temperature to K_s, varied between 10^{-8} ms^{-1} and 10^{-4} ms^{-1}

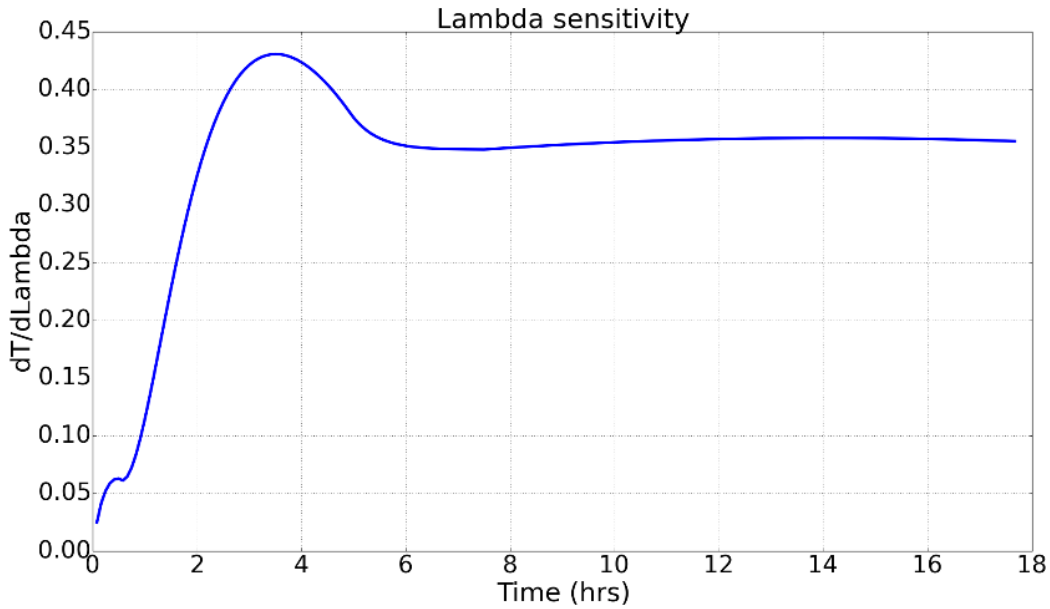

Figure 6: Sensitivity of skin temperature to λ, varied between 2.0 and 6.0

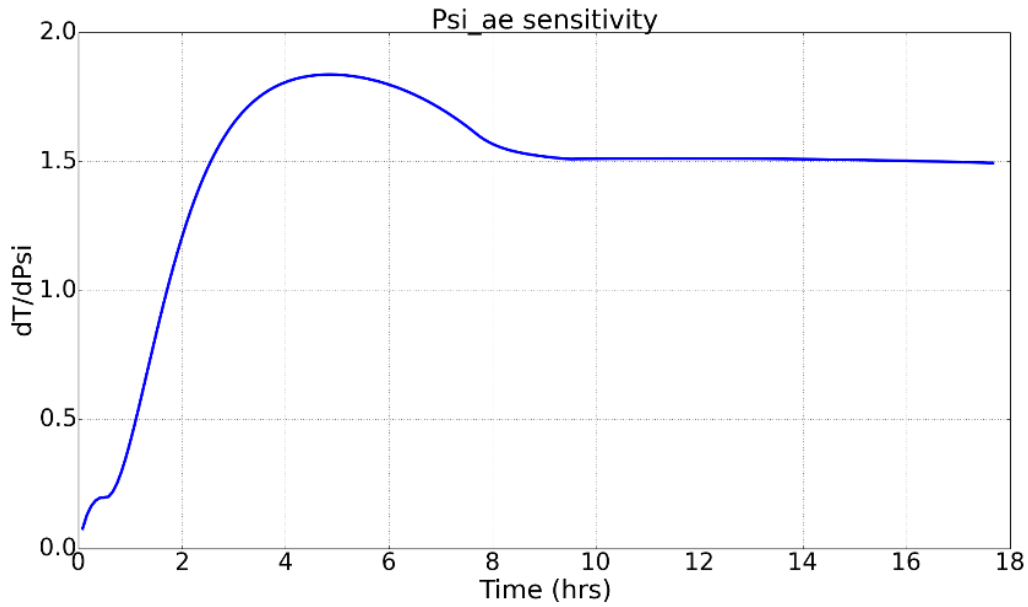

Figure 7: Sensitivity of skin temperature to $\psi_{ae,}$ varied between 0.05 m and 1.45 m

The maximum sensitivity to K_s is 0.25 °C per unit change in K_s, which does not occur until the late times (Figure 5). The maximum sensitivity to λ is 0.43 °C per unit change in λ (Figure 6), and the maximum sensitivity to ψ_{ae} is ~1.8 °C per unit change in ψ_{ae} (Figure 7). Maximum

sensitivity to ψ_{ae} and λ is at earlier times than Ks. The relatively minimal sensitivity of skin temperature to K_s indicates that skin temperature data provides little information on K_s. Attempts to estimate K_s via inversion modeling confirmed this observation. The changes in skin temperature resulting from changes in K_s were not significant enough for the inversion routine to constrain the K_s estimate. Thus, no further attempts were made to estimate K_s using ECH_2O.

Experiment results

The experiments were performed using two different soil types: sand and potting soil. The skin temperature recovery curves for both soil types, collected with the TIR camera, are shown in Figure 8.

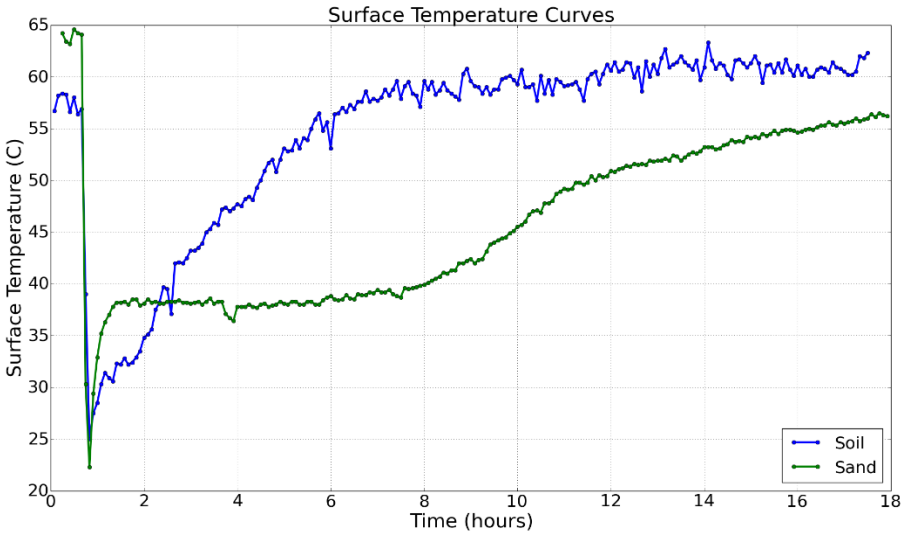

Figure 8: TIR skin temperature recovery curves from each experiment.

The TIR recovery curves show that there is a significant difference in skin temperature recovery between the two soil types tested. This indicates that different soils have different skin temperature responses to and recovery from a wetting event. The response disparity shows that the volume of water in a soil plays a role in determining the bulk thermal properties of the soil, as modeled in Equations 15 and 16. Volumetric water content evolution in an unsaturated soil is controlled by SHPs, showing that SHPs are a controlling factor in skin temperature recovery curves.

Figures 9 and 10 compare the skin temperature data collected with the TIR camera and thermocouple for both sand and soil.

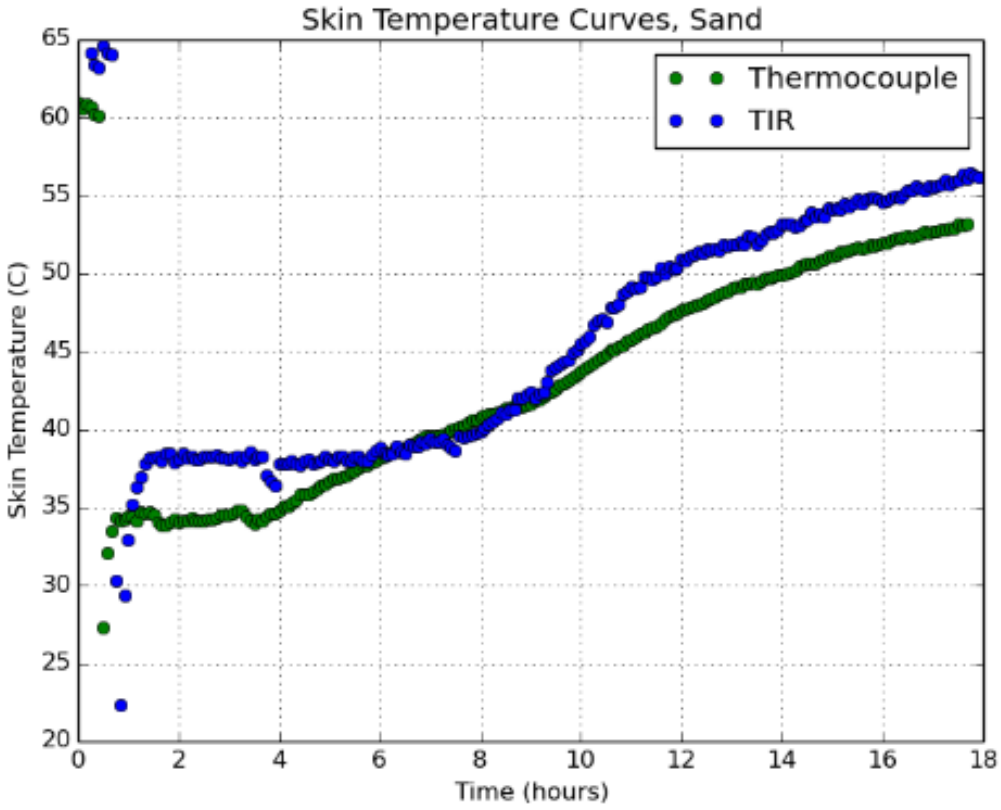

Figure 9: TIR and thermocouple skin temperature curves from the sand experiment

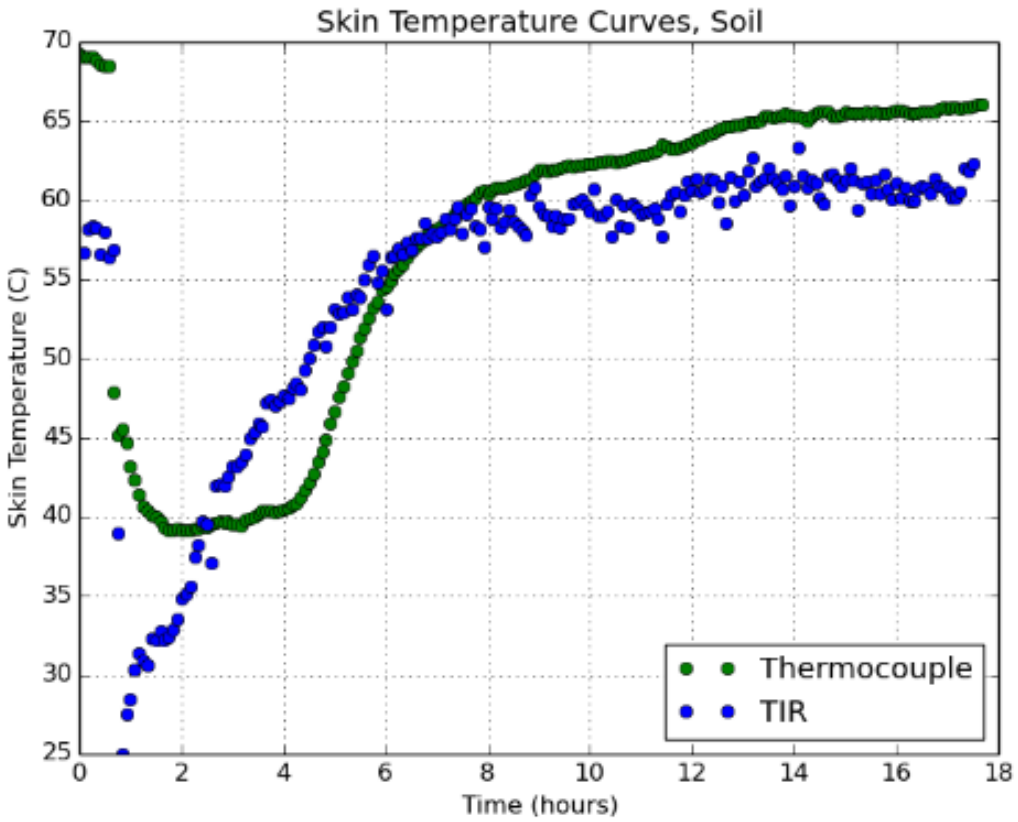

Figure 10: TIR and thermocouple skin temperature curves from the soil experiment

TIR skin temperature recorded from the sand experiment is consistently higher than the thermocouple skin temperature; however, this difference is only a few degrees. The general shape of the two recovery curves match relatively well. TIR skin temperature recorded from the soil experiment shows more variation with respect to the thermocouple data. Skin temperatures in some cases are almost 15 °C different. The shapes of the curves do not match as well either. The TIR curve cools to 25 °C and quickly recovers, while the thermocouple curve cools to 40 °C and remains cool for over 2 hours before beginning to recover to a higher temperature.

Figures 11 and 12 show the temperature data for all in situ sensors in for the sand and soil experiments.

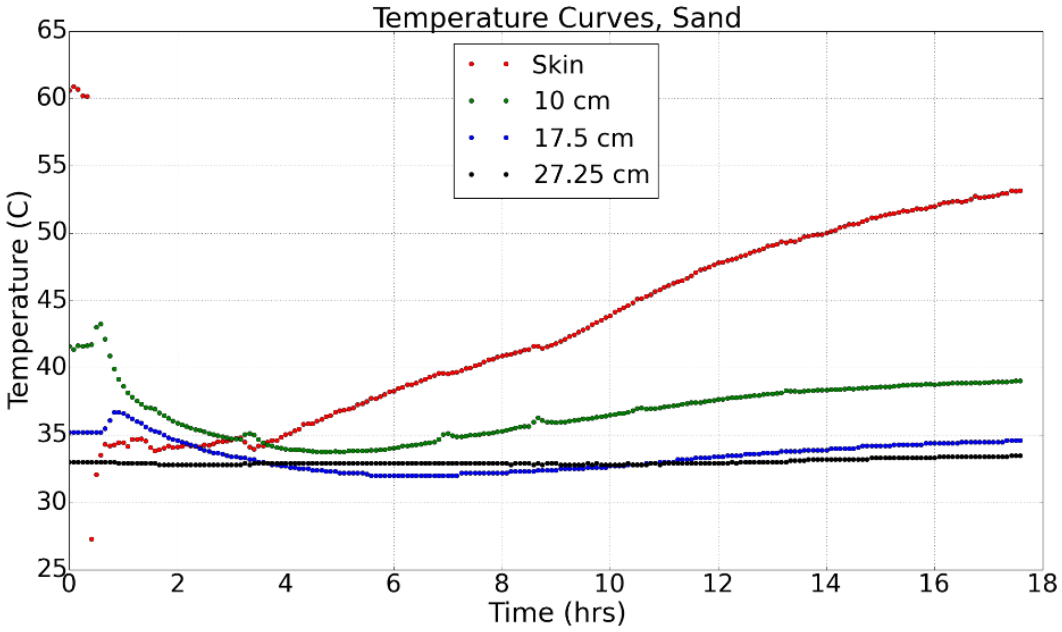

Figure 11: Temperature data from all in situ sensors from the sand experiment

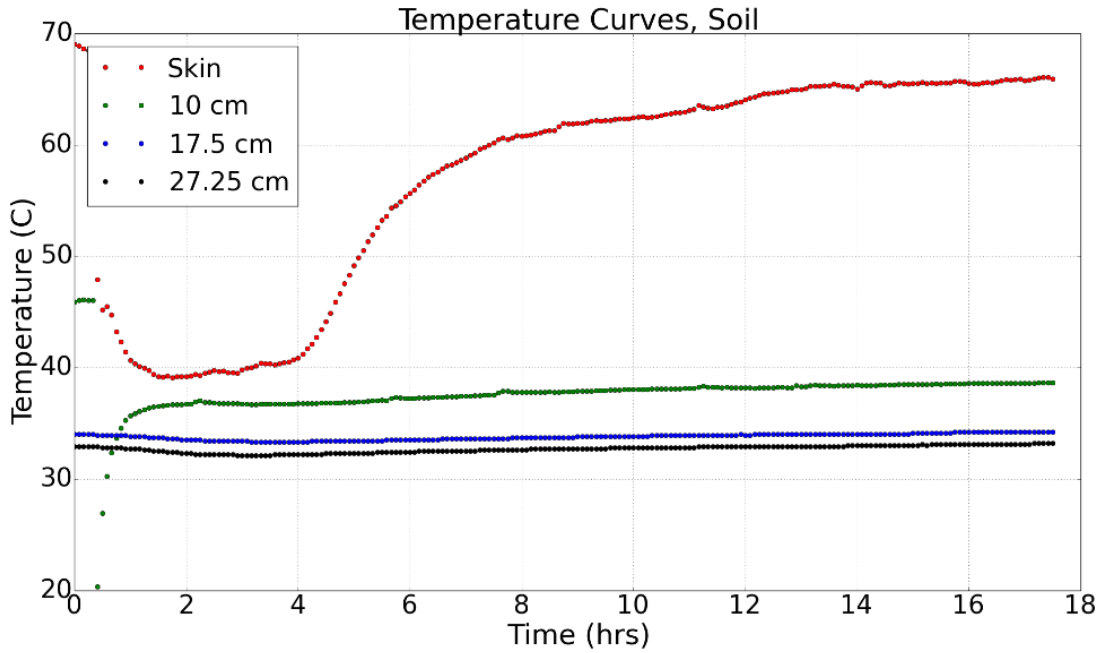

Figure 12: Temperature data from all in situ sensors from the soil experiment

For both experiments, the temperature signal is dampened with increasing depth in the soil column. For the sand experiment, skin temperature rapidly drops to 27 °C before recovering

to 34 °C for 1.5 hours and then steadily recovering. At 10 cm depth, the temperature increases slightly immediately after water application before beginning to decrease over several hours, reaching a minimum of 34 °C 4.5 hours into the experiment and then slowly recovering. At 17.5 cm depth, the temperature shows a similar dampened trend, increasing slightly after water application and then slowly decreasing to a minimum of 32 °C at 5.75 hours. The temperature at 27.25 cm depth remains constant at 33 °C throughout the experiment. In the soil experiment, the skin temperature rapidly drops after water application to 40 °C and remains constant for 2.5 hours before beginning to recover. At 10 cm depth, the temperature rapidly drops to 20 °C, reaching its minimum before the skin temperature curve. It then quickly rebounds to about 37 °C and remains constant for the remainder of the experiment. The temperature at 17.5 cm and 27.25 cm depth remains constant throughout the experiment.

Figures 13 and 14 show the soil moisture data from each experiment. In the sand experiment, soil moisture in the top layer rapidly spiked after water application to a value of 0.24. The top layer drained rapidly until it returned to field capacity 20 minutes after water application, at which point it drained more slowly as capillary forces began to dominate water transport rather than gravitational forces. In the second layer, soil moisture content reached a maximum of 0.145 at 2.5 hours into the experiment, then decreased linearly for the remainder of the experiment. No water drained to the bottommost third layer, which remained constant at 0.06. In the soil experiment, soil moisture content in the top layer quickly increased to a maximum of 0.18 and remained steady for 1 hour before decreasing linearly for the rest of the experiment. Soil moisture content in the second and third layer remained constant at 0.10 and 0.124, respectively. This indicates that no water drained to either layer.

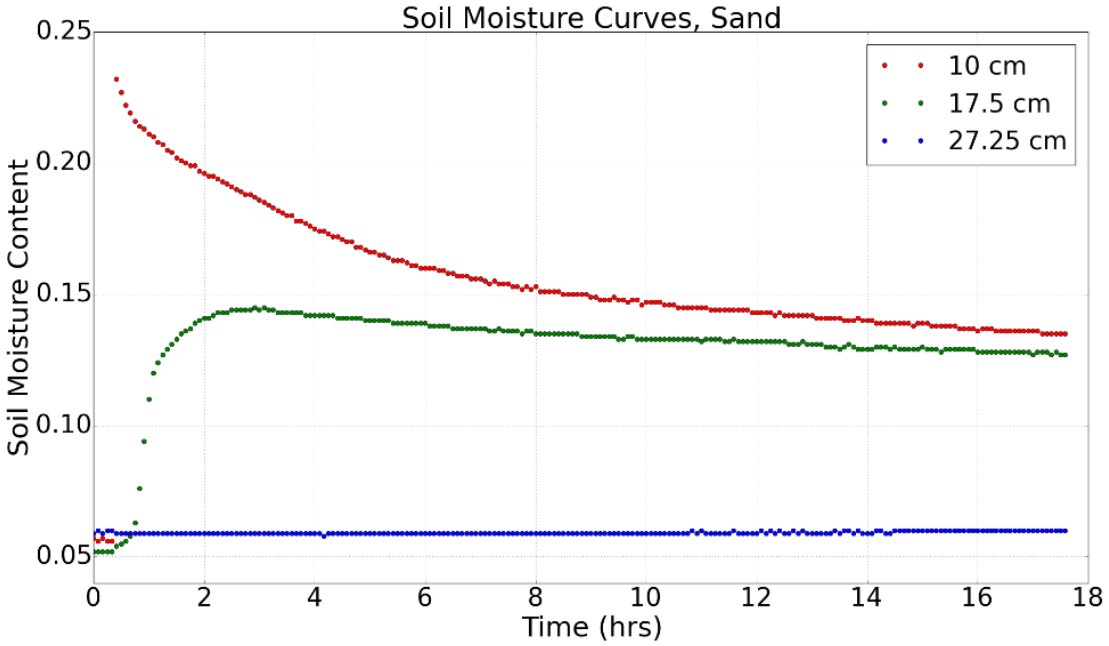

Figure 13: Soil moisture curves from the sand experiment

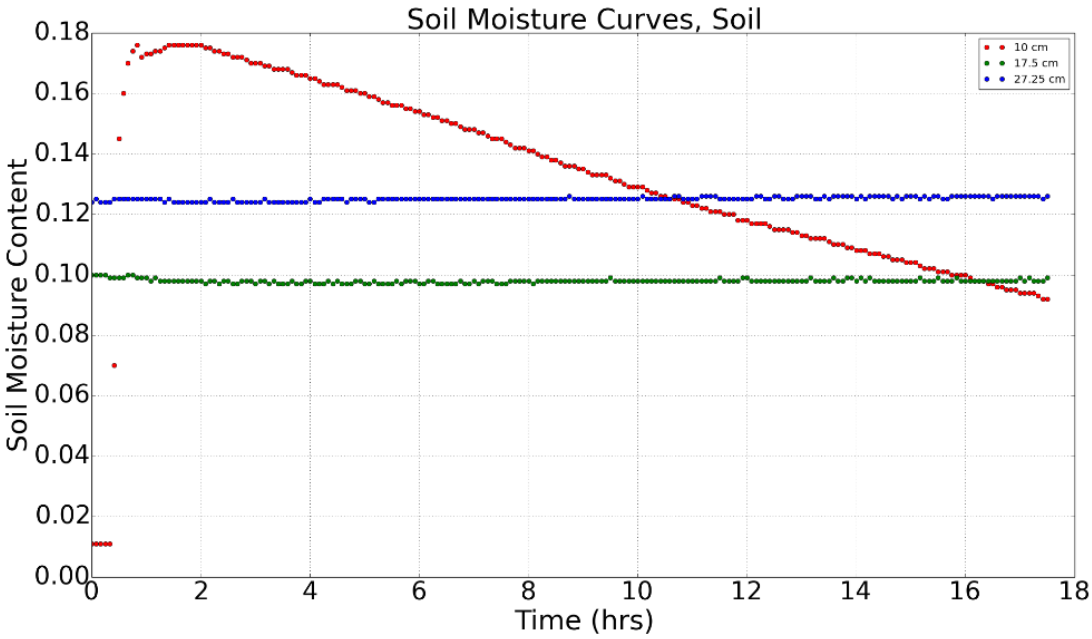

Figure 14: Soil Moisture curves from the soil experiment

Inversion modeling

Inversion was conducted against each TIR data set to determine the average best fit SHP values. Table 2 shows the estimated best-fit SHPs produced by the inversion program, with the 95% linear confidence interval in parentheses. Figures 15 and 16 show the modeled best fit skin temperature and observed skin temperature from the TIR camera for each experiment.

	Sand	Soil
Air-entry pressure, ψ_{ae} (m)	0.243 (20.61%)	0.012 (15.13%)
Brooks-Corey lambda, λ	3.57 (5.53%)	2.95 (3.80%)

Table 2: Best fit SHPs for sand and soil

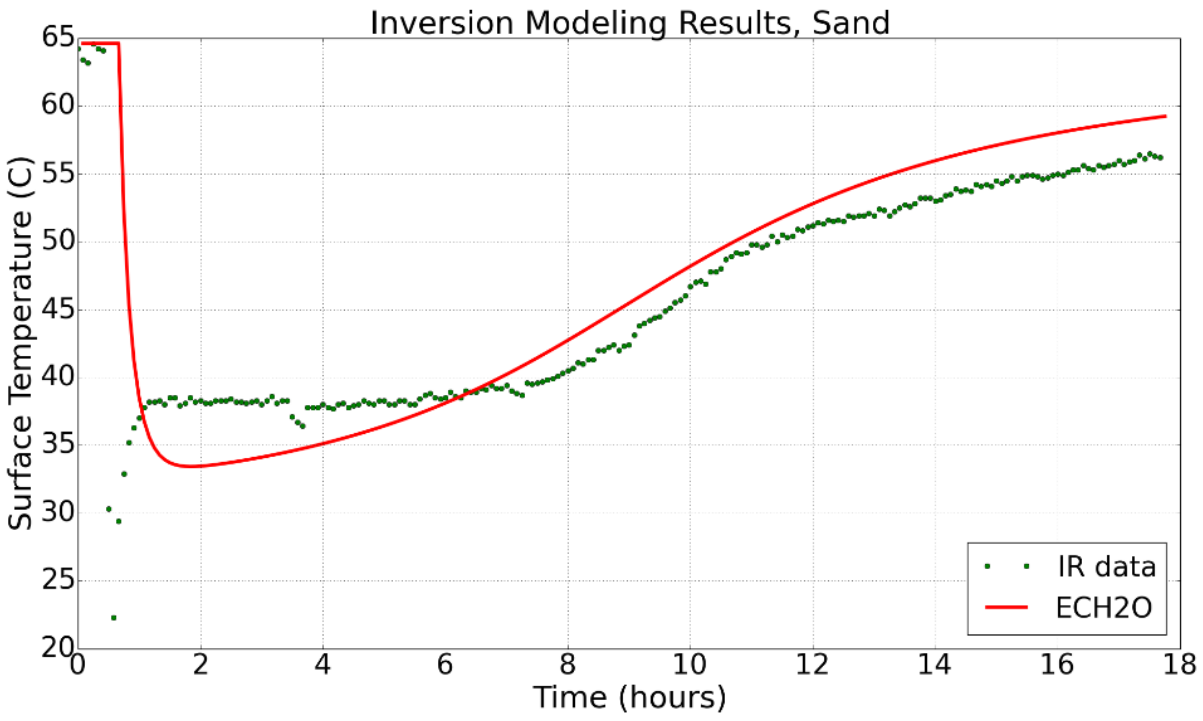

Figure 15: Modeled best fit curve and TIR temperature curve from the sand experiment

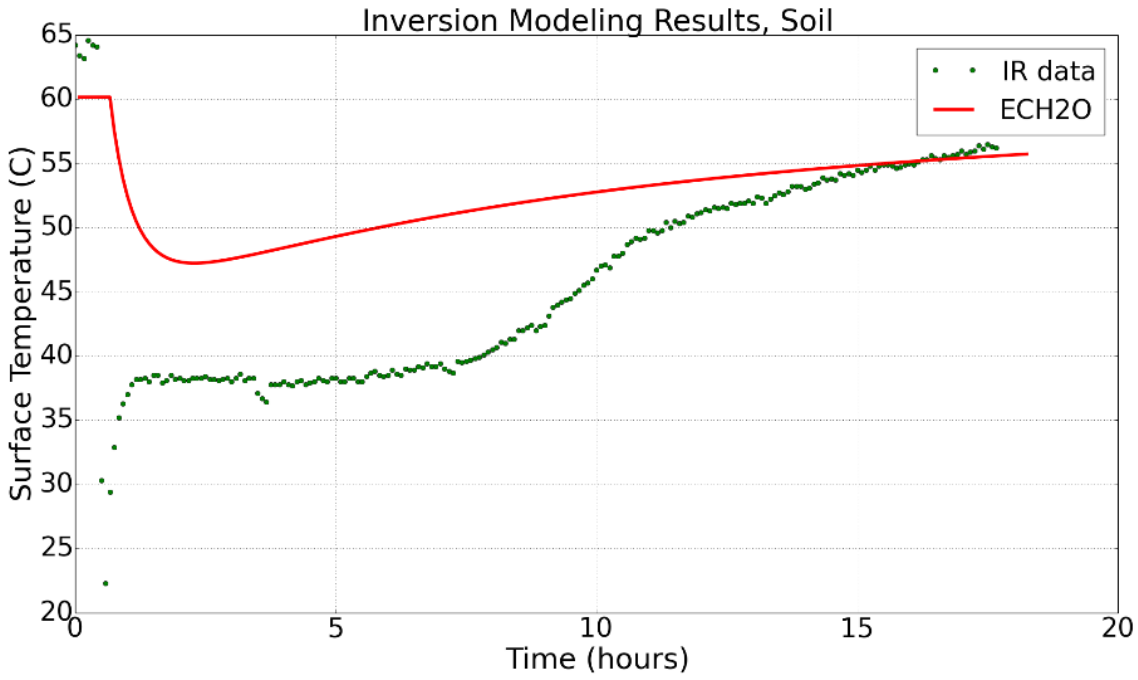

Figure 16: Modeled best fit curve and TIR temperature curve from the soil experiment

The modeled best-fit skin temperature curve for sand, while not exact, has a reasonable fit (Figure 15). While ECH_2O matched the late-time curve shape well, it was unable to model the extremes of the observed skin temperature in the early-time curve immediately after water application. On the other hand, the modeled best-fit skin temperature curve for soil is a poor fit (Figure 16). ECH_2O was unable to model the degree of cooling seen in the observed skin temperature data, instead producing an extremely dampened skin temperature recovery curve. The inversion method was run from multiple starting points to ensure that the minimizer function had not arrived at a local minimum, but each point produced the same result.

Figures 17 and 18 show the resulting modeled soil moisture curves corresponding to the modeled best fit curves. Comparison of the resulting modeled soil moisture curves to the observed moisture profiles provided a test of the accuracy of the SHPs derived from fitting skin temperature. The soil moisture curves for sand show that ECH_2O was able to reproduce the shape of the soil moisture curve for the first layer of the column using the TIR SHP (Figure 17). However, ECH_2O was unable to model the degree of saturation observed in the experiment. Additionally, the ECH_2O model did not show any movement of water into the second layer of sand, as seen in the observed data. The curve for the bottommost layer 3 was well matched.

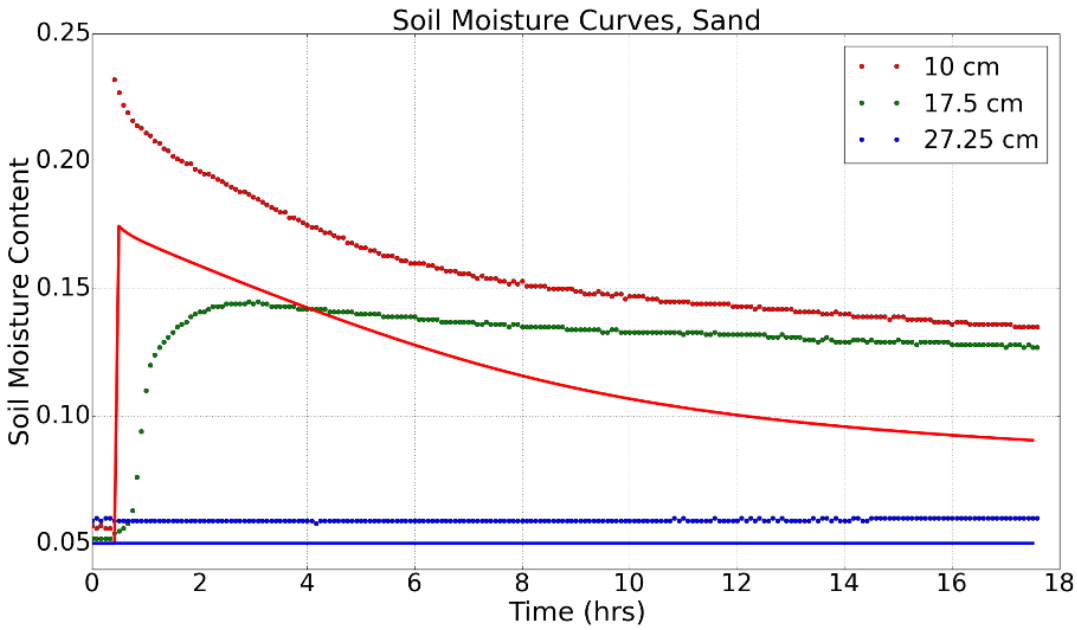

Figure 17: Modeled (solid line) and observed (dots) soil moisture curves from the sand experiment

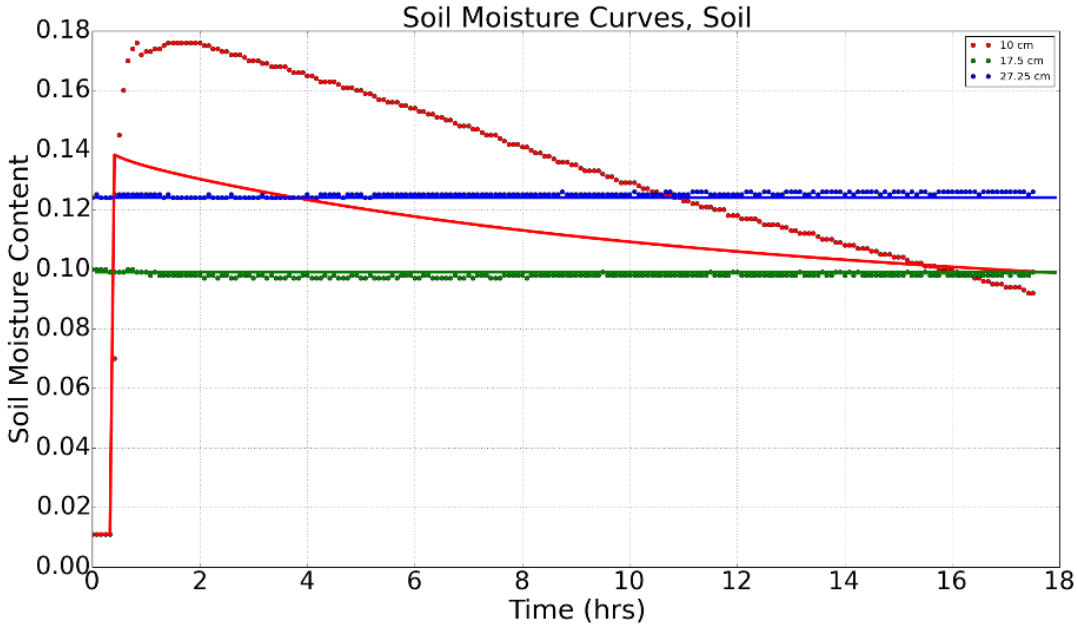

Figure 18: Modeled (solid line) and observed (dots) soil moisture curves from the soil experiment

The modeled soil moisture curves from the soil experiment show different trends. The best fit SHPs caused ECH_2O to output a modeled soil moisture curve that was consistently too

low for layer 1 (Figure 18); however, the difference between the observed and modeled curves for layer 1 was less than that for the sand experiment. The shape of the modeled layer 1 soil moisture curve was inaccurate, however. The modeled soil moisture curves for layers 2 and 3 are consistent with the observed data.

Discussion

The skin temperature recovery curves shown in Figure 8 provide the first indication that estimation of SHPs from surface skin temperature data is feasible. By showing that the thermal response to an identical wetting event under identical conditions varies between two soil types, it is clear that there is a thermal signal which is dependent upon soil type, likely due differences in water movement. The difference between the two curves also suggests that researchers should be able to take advantage of the varying recovery curve shapes to estimate SHP values, given that they control the soil moisture content evolution after a wetting event and thus the bulk thermal properties of the soil matrix. This is supported by Cracknell and Xue (1996), who argue that the identification of soil moisture patterns by thermal inertia mapping is possible. Since soil moisture patterns themselves are controlled by SHPs, identification of spatial variation in temperature should provide insights into SHP values and variation in a landscape.

The inversion method provided estimates of ψ_{ae} and λ with mixed results. Linear uncertainty estimates of the inversion results indicate that SHPs can be estimated based on a soil's characteristic skin temperature recovery signal. The estimated SHP values were compared to several tables of measured SHPs. These results are summarized in Tables 3 and 4.

	Modeled results	Clapp and Hornberger 1978	Cosby et al 1984	Kishne et al 2017
Air-entry pressure, ψ_{ae} (m)	0.243	0.121 ± 0.143 (67.0%)	0.069 ± 0.036 (111.5%)	0.047 ± 0.004 (135.2%)
Brooks-Corey lambda, λ	3.57	4.05 ± 1.78 (12.6%)	2.79 ± 1.38 (24.5%)	3.36 ± 0.30 (6.1%)

Table 3: Comparison of sand SHPs with % difference from modeled values

	Modeled results	Clapp and Hornberger 1978	Cosby et al 1984	Kishne et al 2017
Air-entry pressure, ψ_{ae} (m)	0.012	0.478 ± 0.512 (190.2%)	0.355 ± 0.046 (186.9%)	0.219 ± 0.046 (179.2%)
Brooks-Corey lambda, λ	2.95	5.39 ± 1.87 (58.5%)	5.25 ± 1.66 (56.1%)	6.01 ± 0.80 (68.3%)

Table 4: Comparison of soil SHPs with % difference from modeled values

In general, λ is better matched than ψ_{ae} in both soil types, with both a smaller percent difference from published values and a narrower 95% confidence interval. The set of parameters for sand match those of Clapp and Hornberger (1978), while the parameters for soil match those of Cosby et al (1984). The comparison to other published values suggests that this method provides reasonable estimates of λ for a simple soil type like bare sand. However, the comparison is not near as favorable for the soil λ, and even worse for both ψ_{ae} values. It is also worth noting the variability within the accepted published values. Table 5 shows the percent difference range within the published values for each parameter.

	Sand	Soil
Ψ_{ae}	88.0%	74.3%
λ	18.6%	13.5%

Table 5: % difference between largest and smallest reported SHP values

In most cases, the percent differences between the published parameters is still smaller than the percent differences between the modeled parameters and published values. The wide range of published values reported, along with the error margins on the individual published values, shows the inherent uncertainty and variability involved in measuring SHPs. For instance, the published ψ_{ae} values for sand show an 88% variability, and the variability of ± 0.143 m in the Clapp and Hornberger value is larger than the actual value of 0.121 m.

For sand, Figure 15 and Table 3 show that this method provides reasonable estimates of λ and unreasonable estimates of ψ_{ae}. The best-fit skin temperature curve modeled by ECH_2O is a good match to the observed TIR data and the estimated λ value is well within the range of reported values. However, the ψ_{ae} estimate is significantly larger than the reported values, at times over 100% greater. Figure 16 and Table 4 show that fitting ECH_2O to TIR skin temperature data does not provide accurate SHP estimates for soil. ECH_2O was unable to match

the observed TIR skin temperature curve, and both of the estimated SHP values are significantly lower than those reported by other researchers.

The choice of model may have impacted the estimated SHP results. ECH_2O is primarily an ecohydrologic model that is designed to account for energy and mass conservation across entire ecosystems, and has a significant ecological component built into it. This aspect of the model was disregarded in this study. Additionally, ECH_2O uses the relatively simple Brooks-Corey water retention model to account for water storage in the unsaturated zone. The use of this method with a dedicated variably saturated groundwater model that uses a more robust water retention model, like the van Genuchten, and still includes a surface mass and energy balance calculation could provide better SHP estimates and a better fit to the TIR skin temperature curve. Additionally, the use of the van Genuchten model introduces more SHPs that could potentially be estimated with this method as well.

One of the largest sources of error in the experiment was the emissivity (ε) of the soil material. The fundamental physical relationship that TIR temperature measurement relies on is the Stefan-Boltzmann Law (Equation 22).

$$I = \sigma \varepsilon T^4 \qquad (22)$$

Where I is radiation intensity being emitted from an object (W/m^2), σ is the Stefan-Boltzmann constant ($5.67x10^{-8}$ $Wm^{-2}K^{-4}$), ε is the object's emissivity, and T is the object's temperature (K). Thus, ε is the main variable parameter involved in obtaining temperature from a TIR camera. However, much like SHPs, ε is highly variable both spatially and temporally (Cracknell and Xue 1996). This means ε has a strong effect on the recorded surface temperature of an object (Clark 1976). The emissivity of the soils used in this study was acquired from a lookup table; however, future studies should measure the emissivity of each soil and include it in the image analysis (Faye et al 2015). It is likely that as water leaves the soil surface, the bulk emissivity and thus radiation intensity of the soil material changes. Additionally, Faye et al recommend collecting TIR data during periods of low solar irradiation or at night to prevent interference between solar radiation and radiation emitted from the soil surface.

If successfully developed, this method could drastically speed up the determination of SHPs in field site investigations. Large plots of land could be captured in a single series of

images, with temperature data recorded at each pixel from a TIR camera mounted on a pole or balloon. One image series could be used to estimate heterogeneous SHPs in multiple areas showing different skin temperature signals at once. This would eliminate the need to make multiple infiltrometer measurements in the field to characterize SHP variance. However, future investigations first need to test the applicability of this method in a field setting and for a variety of soil types and vadose zone structures.

Conclusion

In this paper, a method is presented to estimate difficult to measure SHPs from surface skin temperature recorded with a thermal infrared (TIR) camera. This was tested by applying a known volume of water to two different soil columns, one of sand and one of soil, in thermal equilibrium and observing the surface skin temperature recovery curve. A spatially distributed ecohydrologic model was then fitted to the observed curve using inversion modeling in order to estimate ψ_{ae} and λ for each soil type tested. TIR skin temperature data from the experiments show that different soil types exhibit different skin temperature responses to and recoveries from a wetting event. This difference is caused by differences in SHPs, indicating that fitting a model to the skin temperature recovery curves could provide a way to estimate these SHPs. The inversion method was able to provide a reasonable estimate of λ for sand, but was unable to provide reasonable estimates for any of the other SHPs included in the inversion. Overall, this study shows that estimating SHPs from surface skin temperature has the potential to become a useful new tool to properly characterize spatial heterogeneity for some SHPs in field investigations and parameterize numerical models. However, future studies should test this method using dedicated groundwater models and obtain surface emissivity measurements in an attempt to improve the accuracy of the estimated SHPs before evaluating the applicability of this method in the field.

Acknowledgements

The author acknowledges funding provided by the Montana Space Grant Consortium and Dr. Payton Gardner. Special thanks to Dr. Payton Gardner and Dr. Marco Maneta for advising this project, Doug Brugger for providing a thermal camera, and UM BOREALIS for providing inspiration in the early stages this project.

Works Cited

Arya, S. Pal. Introduction to Micrometeorology. San Diego: Academic, 1988. Print.

Babaeian, Ebrahim, Mehdi Homaee, Carsten Montzka, Harry Vereecken, and Ali Akbar Norouzi. "Towards Retrieving Soil Hydraulic Properties by Hyperspectral Remote Sensing." Vadose Zone Journal 14.3 (2015): 0. Web.

Bouwer, Herman. "Rapid Field Measurement of Air Entry Value and Hydraulic Conductivity of Soil as Significant Parameters in Flow System Analysis." Water Resources Research 2.4 (1966): 729-38. Web.

Clancy, Katherine, and Veronica M. Alba. "Temperature and Time of Day Influence on Double-Ring Infiltrometer Steady-State Infiltration Rates." Soil Science Society of America Journal 75.1 (2011): 241. Web.

Clark, J. A. Effects of Surface Emissivity and Viewing Angle on Errors in Thermography. S.l.: S.n., 1976. Print.

Clapp, Roger B., and George M. Hornberger. "Empirical Equations for Some Soil Hydraulic Properties." Water Resources Research 14.4 (1978): 601-04. Web.

Cohen, Matthew, Rao S. Mylavarapu, Ismail Bogrekci, W.s. Lee, and Mark W. Clark. "Reflectance Spectroscopy For Routine Agronomic Soil Analyses." Soil Science 172.6 (2007): 469-85. Web.

Cosby, B. J., G. M. Hornberger, R. B. Clapp, and T. R. Ginn. "A Statistical Exploration of the Relationships of Soil Moisture Characteristics to the Physical Properties of Soils." Water Resources Research 20.6 (1984): 682-90. Web.

Dane, Jacob H., Clarke G. Topp, Jan W. Hopmans, JiÅ™Ã Å imÅ¯nek, Nunzio Romano, and Wolfgang Durner. "3.6.2 Inverse Methods." Methods of Soil Analysis: Part 4 Physical Methods SSSA Book Series (2002): n. pag. Web.

Dingman, S. L. Physical Hydrology. Upper Saddle River, NJ: Prentice Hall, 2002. Print.

Dong, Jianzhi, Susan C. Steele-Dunne, Tyson E. Ochsner, and Nick Van De Giesen. "Determining Soil Moisture and Soil Properties in Vegetated Areas by Assimilating Soil Temperatures." Water Resources Research 52.6 (2016): 4280-300. Web.

Fallow, David James. Measurement of Air Entry and Air Exit Soil Water Pressure Heads with a Modified Guelph Pressure Infiltrometer. Thesis. 1994. N.p.: n.p., n.d. Print.

Fang, Bin, and Venkat Lakshmi. "Soil Moisture at Watershed Scale: Remote Sensing Techniques." Journal of Hydrology 516 (2014): 258-72. Web.

Faye, E., O. Dangles, and S. Pincebourde. "Distance Makes the Difference in Thermography for Ecological Studies." Journal of Thermal Biology 56 (2016): 1-9. Web.

Genuchten, M. Th. Van. "A Closed-form Equation for Predicting the Hydraulic Conductivity of Unsaturated Soils1." Soil Science Society of America Journal 44.5 (1980): 892. Web.

Gutmann, Ethan D., and Eric E. Small. "A Method for the Determination of the Hydraulic Properties of Soil from MODIS Surface Temperature for Use in Land-surface Models." Water Resources Research 46.6 (2010): n. pag. Web.

KishnÃ©, Andrea Sz., Yohannes Tadesse Yimam, Cristine L.s. Morgan, and Bright C. Dornblaser. "Evaluation and Improvement of the Default Soil Hydraulic Parameters for the Noah Land Surface Model." Geoderma 285 (2017): 247-59. Web.

Klute, Arnold, and Herman Bouwer. "Intake Rate: Cylinder Infiltrometer." SSSA Book Series Methods of Soil Analysis: Part 1â□”Physical and Mineralogical Methods (1986): n. pag. Web.

Kondo, Junsei, Nobuko Saigusa, and Takeshi Sato. "A Parameterization of Evaporation from Bare Soil Surfaces." Journal of Applied Meteorology 29.5 (1990): 385-89. Web.

Lee, Tsengdar J., and Roger A. Pielke. "Estimating the Soil Surface Specific Humidity." Journal of Applied Meteorology 31.5 (1992): 480-84. Web.

Liebethal, C., and T. Foken. "Evaluation of Six Parameterization Approaches for the Ground Heat Flux." Theoretical and Applied Climatology 88.1-2 (2006): 43-56. Web.

Mertens, J., H. Madsen, M. Kristensen, D. Jacques, and J. Feyen. "Sensitivity of Soil Parameters in Unsaturated Zone Modelling and the Relation between Effective, Laboratory Andin Situ Estimates." Hydrological Processes 19.8 (2005): 1611-633. Web.

Minasny, B., A. B. Mcbratney, G. Tranter, and B. W. Murphy. "Using Soil Knowledge for the Evaluation of Mid-infrared Diffuse Reflectance Spectroscopy for Predicting Soil Physical and Mechanical Properties." European Journal of Soil Science 59.5 (2008): 960-71. Web.

Pedretti, Daniele, Marco Barahona-Palomo, Diogo Bolster, Xavier Sanchez-Vila, and Daniel FernÃ ndez-Garcia. "A Quick and Inexpensive Method to Quantify Spatially Variable Infiltration Capacity for Artificial Recharge Ponds Using Photographic Images." Journal of Hydrology 430-431 (2012): 118-26. Web.

Petropoulos, George P., Gareth Ireland, and Brian Barrett. "Surface Soil Moisture Retrievals from Remote Sensing: Current Status, Products & Future Trends." Physics and Chemistry of the Earth, Parts A/B/C 83-84 (2015): 36-56. Web.

Price, John C. "The Potential of Remotely Sensed Thermal Infrared Data to Infer Surface Soil Moisture and Evaporation." Water Resources Research 16.4 (1980): 787-95. Web.

R. H. Brooks And A. T. Corey. "Hydraulic Properties of Porous Media and Their Relation to Drainage Design." Transactions of the ASAE 7.1 (1964): 0026-028. Web.

Scholl, M. A., and Scott C. Christenson. Spatial Variation in Hydraulic Conductivity Determined by Slug Tests in the Canadian River Alluvium near the Norman Landfill, Norman, Oklahoma. Oklahoma City, OK: U.S. Dept. of the Interior, U.S. Geological Survey, 1998. Print.

Singh, V. P. Kinematic Wave Modeling in Water Resources: Environmental Hydrology. New York: Wiley, 1997. Print.

Sharma, M.l., G.a. Gander, and C.g. Hunt. "Spatial Variability of Infiltration in a Watershed." Journal of Hydrology 45.1-2 (1980): 101-22. Web.

Steele-Dunne, S. C., M. M. Rutten, D. M. Krzeminska, M. Hausner, S. W. Tyler, J. Selker, T. A. Bogaard, and N. C. Van De Giesen. "Feasibility of Soil Moisture Estimation Using Passive Distributed Temperature Sensing." Water Resources Research 46.3 (2010): n. pag. Web.